Icarus 352 (2020) 113953

Contents lists available at ScienceDirect

Icarus

journal homepage: www.elsevier.com/locate/icarus

Variations of porosity in intermediate-sized lunar impact basins

T.K. Venkatadri [a,*], P.B. James [b]

[a] Massachusetts Institute of Technology, 77 Massachusetts Ave, Cambridge, MA, USA
[b] Baylor University, 1301 S University Parks Dr, Waco, TX, USA

ARTICLE INFO

Keywords:
Moon
Cratering
Geological processes
Porosity

ABSTRACT

The Moon is cratered with hundreds of well-preserved impact basins, and shared bombardment history with Earth makes lunar basins a good proxy for the processes affecting early Earth. Basin-forming impact events alter the bulk density and porosity of the targeted crust, and measurement of these quantities offers a means by which we can investigate the mechanisms of basin formation. In this work, we calculate the bulk density of the crust in the vicinity of 50 basins with diameters of 170–360 km—a size range that has been neglected by previous studies—with the goal of understanding the deformational mechanisms present during impact events. Our bulk density estimates are derived from gravity data from NASA's Gravity Recovery and Interior Laboratory (GRAIL) mission and topography data from the Lunar Orbiter Laser Altimeter (LOLA) using a new technique similar to the Nettleton method in terrestrial gravimetry. By making assumptions about crustal compositions across the Moon, we can furthermore estimate porosity in and around the basins. Low porosity is observed in the interior of 76% of the basins studied, and this trend becomes more apparent when basins in the Feldspathic Highlands Terrane are observed alone. Overall, impact events appear to decrease porosity inside basins and increase porosity outside basins, suggesting the prevalence of impact melting within the basins and fracturing and ejecta deposition in the exteriors. Our results are seemingly inconsistent with previous studies that measured high porosity values inside basins from residual Bouguer anomalies. However, these disparate results may be reconciled if impact melting processes are confined to the uppermost kilometers of the lunar crust and are underlain by heavy impact-induced fracturing.

1. Introduction

The Moon and Earth have experienced similar histories of bombardment. However, Earth has undergone resurfacing events that have removed much of the ancient surface (Johnson and Bowling, 2014). In contrast, the lack of erosion on the Moon, especially in highlands regions such as the Feldspathic Highlands Terrane (FHT) (Jolliff et al., 2000), preserves ancient rock (Andrews-Hanna et al., 2013). By studying lunar highlands rock properties, it may be possible to understand phases of Earth's history that have been erased by erosion and develop a timeline of events that affected the early Solar System (Blewett et al., 2002). Recent NASA missions, including the Gravity Recovery and Interior Laboratory (GRAIL; 2012), Lunar Orbiter Laser Altimeter (LOLA; 2009), and Lunar Prospector (1998), have provided high-resolution data of ancient rock features located in the lunar highlands.

Among other properties, the variations in chemical composition and porosity (the fraction of empty space in the rock) across the lunar crust may be derived from these data sets. The chemical composition of the lunar highland surface, represented as the grain density, has been charted extensively in the past (Gillis et al., 2004; Wieczorek et al., 2013). If the composition of the crust is known, the crustal porosity may be inferred from gravitationally-derived bulk density (Besserer et al., 2014; Huang and Wieczorek, 2012; Wieczorek et al., 2013). The preserved porosity signatures of the basins can be used to understand the cratering process and the different phenomena present during impact events that shaped the Moon, and, by extension, Earth.

Opposing mechanisms during an impact event may either increase or decrease the porosity in the vicinity of a basin as it forms. In the processes of fracturing and dilatancy, the asteroid may shatter the rock on impact and cause the rock fragments to volumetrically expand, increasing the porosity (Collins, 2014). Particularly for larger impacts, the zone of fracturing may extend well beyond the basin rim and increase the porosity throughout the crust in the region surrounding the basin (Wiggins et al., 2019). In addition, impact ejecta may be deposited on the rim of the basin, increasing the porosity immediately outside the

* Corresponding author at: Massachusetts Institute of Technology, 77 Massachusetts Avenue, Cambridge, MA 02139, USA.
E-mail address: tkvenkat@mit.edu (T.K. Venkatadri).

https://doi.org/10.1016/j.icarus.2020.113953
Received 1 February 2020; Received in revised form 24 June 2020; Accepted 25 June 2020
Available online 5 July 2020
0019-1035/© 2020 Elsevier Inc. All rights reserved.

basin by covering the surface with loosely-compacted rock fragments (Soderblom et al., 2015). Alternatively, in the process of impact melting, the heat of the impact event may cause the rock to melt and deform, sealing pre-existing pore spaces and decreasing porosity (Milbury et al., 2015). By charting the variations in porosity, it may be possible to understand which mechanisms were dominant in different areas of ancient impact basins.

Several methods have previously been used to determine the porosity in lunar basins of various sizes (Neumann et al., 2015). One study (Soderblom et al., 2015) examined porosity trends associated with basins and craters with diameters between 20 and 200 km in the lunar feldspathic highlands, and found high porosities in the interiors of these small basins. Soderblom et al. measured the difference in the Bouguer anomaly at the center of a crater versus an average Bouguer anomaly in an external annulus, and these measured differences were assumed to result from variations in porosity. Uplift of the mantle under a crater would also produce such a difference in the Bouguer anomaly, so the methodology of Soderblom et al. is only appropriate for characterizing porosity in craters with no significant mantle uplift. Consequently, this methodology is only appropriate for craters with diameters smaller than approximately 200 km.

Spatio-spectral techniques using localized gravity–topography spectra have also been employed to determine the distribution of porosity (Besserer et al., 2014; Wieczorek et al., 2013). These studies used sophisticated eigenvalue calculations and windowing functions called "Slepian tapers" to maximize signal power within a desired region while minimizing spectral leakage (Dahlen and Simons, 2008). A benefit of this approach is that it preserves the relationship between effective density and the spherical harmonic degree l, which allows the distribution of porosity with depth to be inferred (Besserer et al., 2014). However, these spectral characterizations come at a cost: the analysis requires a relatively large localization window. Wieczorek et al. used circular localization windows that spanned 12° of latitude, or 364 km. This technique resulted in observations of relatively low porosities in the interiors of some basins, but the diffuse nature of the Slepian tapers make this method ill-equipped to resolve porosity variations in all but the largest basins.

Porosity in intermediate-sized basins can be determined through a new methodology based on the Nettleton method (Nettleton, 1939). The Nettleton method is widely used in terrestrial settings to estimate bedrock density over short baselines, and the GRAIL and LOLA missions provided the first sufficiently high-resolution data necessary to use this method to analyze lunar rock (Smith et al., 2010; Zuber et al., 2013). The methodology – along with the theory of gravity-topography correlation derived in Wieczorek and Phillips (1998) – can be used to calculate bulk density in basins of any diameter. We previously performed a proof-of-concept study, using this methodology to study porosity in three highland basins: the Hertzsprung, Korolev, and Freundlich-Sharonov basins (Venkatadri and James, 2017). We calculated bulk density every 60 km within these basins through a least-squares fit between GRAIL and LOLA data. To isolate density variations resulting from porosity changes, we corrected the bulk density values based on empirically derived relationships between bulk density and iron content, as well as bulk density and topography. We found low porosities in the basin interiors compared to the exteriors, consistent with the findings of Wieczorek et al. (2013). Given that these methods are closely related to those of Wieczorek et al. (2013), we concluded that the methods outlined by Wieczorek and Phillips (1998) are viable for calculating porosity. Therefore, they may be used to map the porosity variations in basins with a diameter between 200 and 360 km, since porosity in basins of this size range has not yet been analyzed (we did not consider larger basins because the Wieczorek et al. (2013) results already accounted for basins with a diameter over 360 km).

Our first goal in this study was to apply the new methodology to understand the changes in porosity in basins with diameters between 170 and 360 km. This includes the upper part of the diameter range studied by Soderblom et al. (2015) as well as the smallest basins resolvable with spatio-spectral localization (Wieczorek et al., 2013). Building on these previous studies of other lunar basins, we hypothesized that porosity would be significantly different in the interior and exterior of the basins in this size range, although we were not sure which porosity would be greater. We planned to use our findings to understand the physical phenomena affecting porosity within and immediately outside intermediate-sized basins.

Our second goal was to observe the trends in porosity with respect to basin diameter. Soderblom et al. (2015) reported that crustal porosity is relatively high inside basins with a diameter less than 200 km, whereas Wieczorek et al. (2013) reported that porosity is relatively low within basins with a diameter over 360 km. We therefore hypothesized that there would be a threshold diameter range in which the porosity trend in the basins switched, thereby reconciling these seemingly disparate conclusions.

Our third goal was to determine whether porosity is related to basin age. Throughout lunar history, different preimpact porosities, temperatures, and rates of bombardment may have conceivably influenced the porosity of the crust in the vicinity of impact basins (Milbury et al., 2015; Miljković et al., 2013). We hypothesized that the conditions of basin formation during different time periods in lunar history would result in different average porosity across the basins formed in each epoch.

2. Methodology

2.1. Data sets and topographic correction of gravity values

The weighted least-squares fit methodology we applied as a modified version of our previous work (Venkatadri and James, 2017) relied on data sets from the GRAIL and LOLA missions. The GRAIL data (Zuber et al., 2013) mapped gravity anomalies, and the LOLA data (Smith et al., 2010) mapped topography. The expected free-air gravity anomaly that would be produced by topography—which we call "gravity-from-topography"—may be determined using a calculation involving powers of topography (Wieczorek and Phillips, 1998). The gravity-from-topography is proportional to the density of the lunar crust, which is unknown, so for the purpose of our analysis a density value of 1 g/cc is arbitrarily chosen (this unitary density has no bearing on the final calculated density). In essence, the density calculations described in Section 2.3 will seek to determine the true rock density that makes the gravity-from-topography match the observed gravity anomaly.

Before data sets of gravity and gravity-from-topography can be used to determine the density of a terrain, both must be carefully prepared to suit our analysis. The first step is to determine an appropriate "reference radius" R_0 (i.e., a constant distance from the Moon's center of mass) for a given region. The Moon's external gravity field is a potential field that obeys Laplace's Equation, and as a result, the gravity field at one reference radius can be inferred from the gravity field at another reference radius. Lunar gravity data products generally choose a value of $R_0 = 1738$ km since this is approximately equal to the Moon's average radius, but for most regions on the Moon, this value of reference radius is significantly above or below the actual topography. A poorly chosen reference radius would change the spectral characteristics of the resulting gravity field, as is illustrated in Fig. 1 for a basin-free section of the lunar far-side highlands. Topography relative to $R_0 = 1738$ km is plotted in Fig. 1a, and the average topography in this region has a radius of approximately 1742 km from the center of the Moon. When this average value is chosen as the reference radius, the spectral characteristics of the resulting gravity field are similar to those of topography (Fig. 1c). If instead the gravity field is downward-continued to a reference radius that is below the mean topography ($R_0 = 1738$ km, Fig. 1b), the gravity field becomes "noisy" and is dominated by short-wavelength variability. If the gravity field is upward-continued to a reference radius that is significantly above the mean topography ($R_0 = 1755$ km, Fig. 1d),

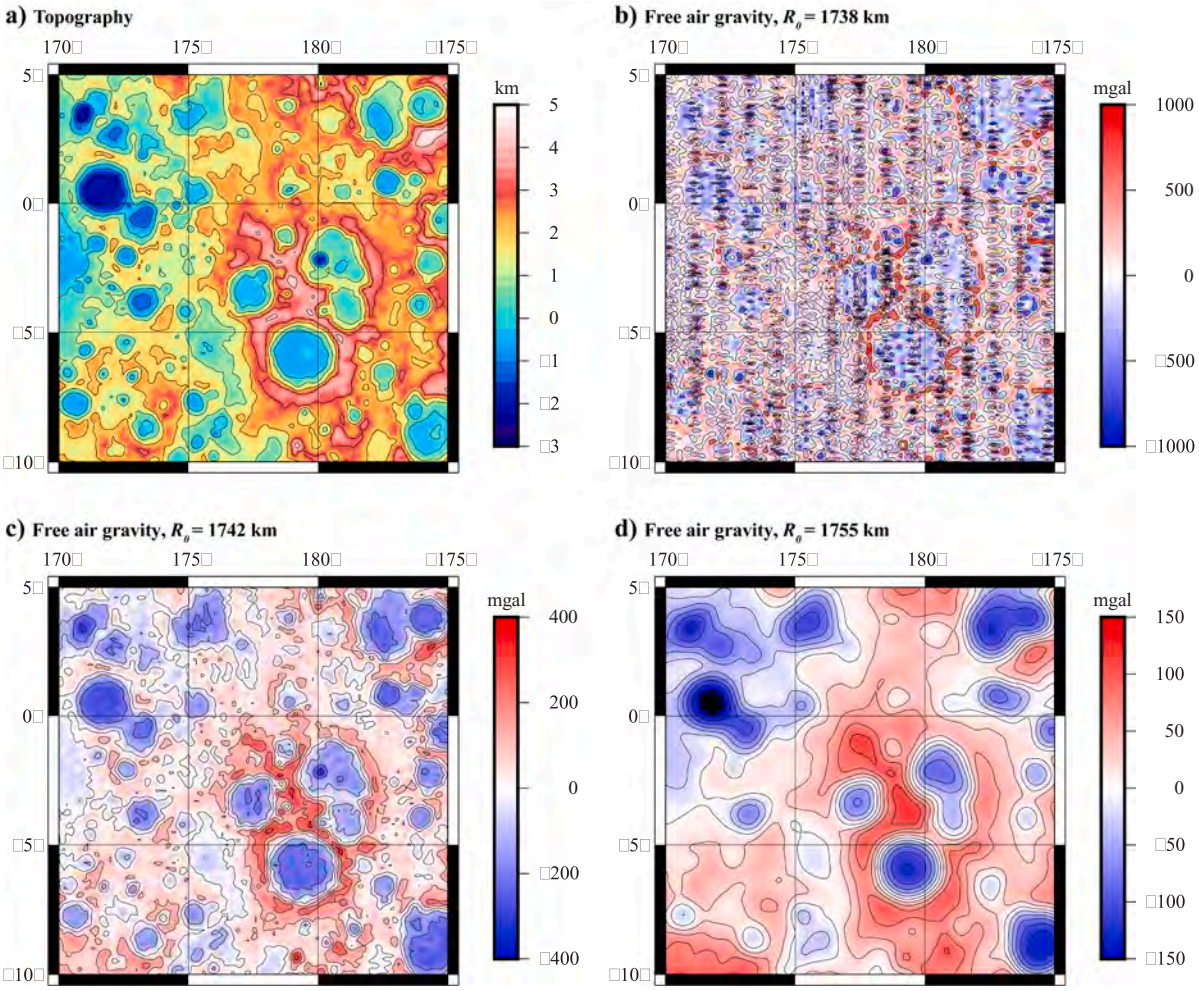

Fig. 1. Demonstration of the effect on the chosen reference radius R_0 on the resulting free-air gravity anomaly. (a) Topography of a basin-free section of the lunar farside highlands. (b) Free-air anomaly in the same region, referenced to a radius $R_0 = 1738$ km. Note that this choice of reference radius results in "noisy" data in which the high-frequency portion of the signal has a relatively large amplitude. (c) Free-air anomaly referenced to a radius $R_0 = 1742$ km. Note that this choice of reference radius results in gravity that has spectral characteristics similar to those of topography. (d) Free-air anomaly referenced to a radius $R_0 = 1755$ km. Note that this choice of reference radius emphasizes the long-wavelength portion of the gravity field and suppresses the short wavelength portion of the field.

the gravity field becomes relatively smooth and is dominated by long-wavelength variability. These spectral characteristics of the gravity fields are important because different wavelengths of gravity are sensitive to different depths in the lunar interior (Besserer et al., 2014), and the bulk density of the lunar crust generally increases with depth. Consequently, gravity analyses at different locations will be sensitive to the same depth-distribution of porosity if they adopt reference radii that are customized to the local topography (cf. Section 2.4).

The second important aspect of gravity data preparation is spectral filtering. At spherical harmonic degrees less than approximately $l = 100$, the lunar gravity field is influenced by the crust-mantle interface. If the crust-mantle interface is negatively correlated with topography, as would be expected for isostatic compensation of lunar topography (Sori, 2018), the mantle contribution to the lunar gravity field would introduce a downward bias on the measured densities. Since we wish to avoid this source of bias, we partially suppress the portion of the gravity field associated with spherical harmonic degrees less than $l = 250$ and completely remove the portion of the gravity field associated with spherical harmonic degrees less than or equal to $l = 150$ (Eq. 1). Gravity anomalies associated with spherical harmonic degrees higher than approximately $l = 700$ have significant errors, since the error power spectrum exceeds the signal power spectrum at this degree and the signal-to-noise ratio for the data set drops below 1:1. In order to prevent data error from influencing our analysis, we start filtering for gravity associated with spherical harmonic degrees larger than $l = 600$ and completely remove all gravity associated with degrees greater than $l = 700$. This filter and the previously described low-degree filter are encapsulated in the following piece-wise equation:

$$\omega(l) = \begin{cases} 0, & l \le 150 \\ \frac{1}{2}\left[-cos\left(\pi\frac{l-150}{100}\right)+1\right], & 150 \le l < 250 \\ 1, & 250 \le l < 600 \\ \frac{1}{2}\left[cos\left(\pi\frac{l-600}{100}\right)+1\right], & 600 \le l < 700 \\ 0, & l \ge 700 \end{cases} \quad (1)$$

We multiply the gravity and the gravity-from-topography data by this degree-dependent filter, $\omega(l)$, in order to isolate the signals that are most useful for density estimation.

This filter does not perfectly eliminate the gravitational effects of the lunar mantle, but the influence of the mantle should be small: for a local crustal thickness of 40 km, the presence of isostatic crust–mantle interface relief would cause us to underestimate the bulk density of the crust by 0.3% at spherical harmonic degree $l = 250$, and it would cause

us to overestimate the local porosity by a similar amount. Even so, the rigidity of the Moon's lithosphere does not necessarily require the existence of compensation at such short wavelengths (Audet, 2014). Thus, we can be reasonably confident that the lunar mantle is not causing significant errors in our porosity measurements.

2.2. Basins and data weighting scheme

Using a lunar crater database (Losiak et al., 2009), 50 basins within the diameter range of 170 to 360 km were initially selected for analysis. We further divided each basin into three concentric annular zones, as depicted in Fig. 2. The "interior" zone is defined as the terrain within 80% of a basin's radius from the center of the basin (shown in white), the "rim" zone is defined as the terrain between 80% and 120% of a basin's radius (shown in gray), and the "exterior" zone is defined as the terrain between 120% to 160% of a basin's radius (shown in black).

The vicinity of each basin is divided into square 100 km × 100 km regions, or "pixels," for the purpose of the density and porosity analysis in Section 2.3. The entirety of each pixel is assigned to the nearest zone, as shown in Fig. 2. Since gravity and gravity-from-topography are sensitive to changes in topography, we generated new gravity and gravity-from-topography maps for each zone of each basin with a reference radius R_0 equal to the average topography within the zone. As described in Section 2.1, this methodological step is crucial: it ensures that the spectral properties of the gravity anomalies and the associated depth sensitivity are consistent between zones of different elevations.

Furthermore, we define a weighting function w within each pixel in order to weight data at the center of the pixel more heavily:

$$w(x,y) = cos^2\left(\frac{\pi}{100}(x-x_0)\right)\cdot cos^2\left(\frac{\pi}{100}(y-y_0)\right), -50 \le x,y \le 50 \quad (2)$$

where x and y are the Cartesian coordinates within a pixel, with units of kilometers, and x_0 and y_0 are the coordinates of the center of the pixel, also with units of kilometers. This tapered weighting function avoids undesirable edge effects that are often associated with boxcar tapers (Thompson and Tree, 1980; Dahlen and Simons, 2008). If the pixels are allowed to overlap by 50 km, this particular taper design has the added benefit of producing uniform data coverage (i.e., the sum of the taper weights at any given point equals one). This overlapping configuration allows us to measure bulk density on a 50 km × 50 km equirectangular grid, as shown in Fig. 2 and in Appendix A.

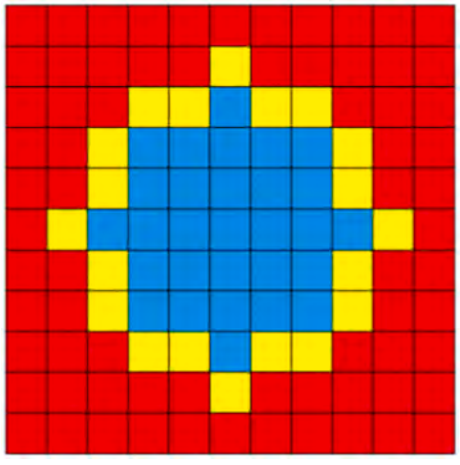

Fig. 2. Annular interior, rim, and exterior regions on a sample grid (where each square represents a 50 km × 50 km region). White indicates regions within the basin interior (<80% of basin radius), grey indicates the basin rim (80–120% of basin radius), and black indicates the basin exterior (>120% of basin radius).

2.3. Calculation of bulk density and porosity in craters

Nettleton (1939) outlined a method for calculating the bulk density of a terrain using ground-based gravimeter measurements. This method exploits the fact that the Bouguer anomaly on a gently sloping terrain is a linear function of the bedrock density. The relationship between density and observed gravity becomes more complicated in the vicinity of steeply sloped terrain, but Parasnis (1952) and others showed that the appropriate density could be determined through an iterative calculation. Methods of varying complexity that exploit the relationship between gravity and topographic density are called "Nettleton methods", and variations of the Nettleton method have been widely used in terrestrial geophysics (cf. Yamamoto, 1999, and references therein).

With the exception of the Apollo 17 Traverse Gravity Experiment (Talwani et al., 1973), gravity data on the Moon comes exclusively from orbit, tens or hundreds of kilometers above the surface. Although lunar gravity data are not ground-based, we can devise an analysis method that is nonetheless comparable to the Nettleton method. Since gravity data and predicted gravity-from-topography can be plotted at a uniform radius R_0, the inference of density is, in some ways, simpler than the traditional Nettleton method. If GRAIL free-air gravity values (of which an individual sample is labeled "g_i") are plotted on the y-axis and LOLA-derived gravity-from-topography values ($\hat{g}_i$) are plotted on the x-axis, the bulk density is simply the best-fit slope. Expressed as a linear model, this is:

$$g_i = \rho\,\hat{g}_i + b \quad (3)$$

where ρ is the bulk density and b is the y-intercept (somewhat unimportant for this analysis). The least squares slope for the data set can be calculated using various sums involving these terms. It is useful to first calculate two scalar "sum-of-squares" quantities:

$$S_1 = \sum_{i=1}^{n} w_i (g_i - \bar{g})\left(\hat{g}_i - \bar{\hat{g}}\right) \quad (4)$$

$$S_2 = \sum_{i=1}^{n} w_i \left(\hat{g}_i - \bar{\hat{g}}\right)^2 \quad (5)$$

where n is the number of sampled points and $\bar{g}$ and $\bar{\hat{g}}$ are the weighted mean values of gravity and gravity-from-topography (using the weighting scheme described in Eq. 2), respectively:

$$\bar{g} = \frac{\sum_{i=1}^{n} w_i g_i}{\sum_{i=1}^{n} w_i} \quad (6)$$

and

$$\bar{\hat{g}} = \frac{\sum_{i=1}^{n} w_i \hat{g}_i}{\sum_{i=1}^{n} w_i} \quad (7)$$

The least-squares slope is the quotient of these two sum-of-squares quantities:

$$\rho = \frac{S_1}{S_2} \quad (8)$$

In order to quantify the uncertainty of the least-squares slope, note that the y-intercept b is related to the weighted means of gravity and gravity-from-topography:

$$b = \bar{g} - \rho\bar{\hat{g}} \quad (9)$$

Now we can define a third sum-of-squares quantity using the best-fit model parameters ρ and b:

$$S_3 = \sum_{i=1}^{n} w_i \left(g_i - \left(\rho\hat{g}_i + b\right)\right)^2 \quad (10)$$

This is essentially the sum of the squares of the errors between the data and the regression line. Now we can calculate the standard error (E) of the slope measurement:

$$E = \frac{\sqrt{S_3/S_2}}{D} \tag{11}$$

where D is the degree of freedom for the local gravity data, which we treat as the number of employed spherical harmonic coefficients divided by the fractional surface area of one pixel relative to the global surface area. Since E corresponds to the standard error of the slope of the least-squares regression, the 95% confidence interval for the bulk density in a pixel is given by $\rho \pm 2E$.

Bulk density varies based on porosity and grain density, so porosity values for a region may be isolated from bulk density values by controlling the grain density. Using a grain density map created by Wieczorek et al. (2013) from the Lunar Prospector mission, we created a data set that estimated grain density every 5 km in each basin. We calculated the weighted mean grain density for each pixel using the same weighting scheme as the least-squares fit, then determined porosity from the grain density and bulk density in every pixel (Eq. 12). In the equation, ρ_{bulk} is the bulk density from the weighted least-squares fit in g/cc, ρ_{grain} is the weighted average grain density in g/cc, and φ is the porosity as a decimal portion of volume.

$$\rho_{\text{bulk}} = \rho_{\text{grain}} \cdot (1 - \varphi) \tag{12}$$

From the density confidence intervals, we generate a confidence interval for each porosity measurement, where the new error is:

$$E_{\text{porosity}} = E_{\text{bulk density}} / \rho_{\text{grain}} \tag{13}$$

We used the porosity values to generate porosity maps of interior, rim, and exterior for each basin, in order to illustrate the high-resolution porosity variations in crater regions.

2.4. The recipe for bulk density estimation

Here we will outline the recipe with which a researcher can estimate the bulk density of a given region on the Moon. This is the process that we used in our investigation, and we hope that it can be adapted by future researchers for a variety of investigations into the density of lunar terrains.

Step 1: Identify and delineate a region of interest. Due to the broad nature of our current investigation, we chose to use simple square-shaped regional tapers (i.e., the "pixels" described in Section 2.2). However, a taper can be arbitrarily shaped, with the caveat that topologically complex tapers are more susceptible to undesirable edge effects. The terrain within a taper should be as geologically uniform as possible; for example, a taper that spans a basaltic mare deposit as well as a feldspathic terrain might yield an unrealistic bulk density estimate.

Step 2: Choose a reference radius. For this investigation, we chose three different reference radii for each taper corresponding to the floor, rim, and exterior of each basin, and the reference radii were chosen to coincide with the mean height of topography in each region, in accordance with the Nettleton method. Different criteria may be used for selecting the reference radii—for example, one could choose a reference radius 2 km above the mean topography—but it is important to apply such a criterion consistently across all regions of study.

Step 3: Determine the ideal spectral band-pass for the gravity maps. Our method assumes no contribution to the gravity field from the crust–mantle interface, so the lower limit of the band-pass must be sufficiently large to make the contribution from the crust–mantle interface negligible (see Section 2.1). We use a lower limit of $l = 250$ for the investigation in this paper, but a reduced lower limit would be defensible in regions with thicker crust. At the present time, the requirement of such large spherical harmonic degrees and orders prevents us from applying our method to any planetary bodies other than the Moon or Earth. The upper limit for the band pass should correspond to the degree strength of the gravity field, i.e., where the power of the uncertainty exceeds that of the signal.

Step 4: Render the free-air gravity and the expected gravity-from-topography. The free-air gravity anomaly can be derived from spherical harmonic coefficients on the Geosciences Node of the Planetary Data System (https://pds-geosciences.wustl.edu/), and spherical harmonic coefficients of a planet's topography may be found there as well. The formula for converting coefficients into the free-air anomaly for a given reference radius is described in Wieczorek (2007). Similarly, gravity-from-topography may be derived from topography coefficients using the finite-amplitude formula described in Wieczorek and Phillips (1998). Some scripts for performing these calculations are available within SHTOOLS (Wieczorek and Meschede, 2018) or the SLEPIAN software suite (Harig et al., 2015).

Step 5: Calculate the best-fit bulk density. This may be performed using the least-squares methodology described in Section 2.3.

2.5. Porosity trends

We also aimed to analyze the trends in average porosity as a function of each of the following three quantities: distance from the basin interior, basin diameter, and basin age. To perform this, we performed a regular, unweighted least-squares fit for all datapoints in the circular interior, rim, and exterior regions. Porosity values and confidence intervals were calculated for these three regions based on bulk density (the slope of the line of best fit) and grain density (from Lunar Prospector) (Eqs. 3–13, where new degrees of freedom are based on the total areas of the interior, rim, and exterior zones).

We determined the porosity contrast for each basin as the difference between the exterior and interior porosities (Eq. 14), with the rim porosity excluded because the rim is a transitional region and may be affected by various physical phenomena that act on both the interior and exterior. The porosity contrast $\Delta\varphi$ is defined below (all porosity values expressed as percentages):

$$\Delta\varphi = \varphi_{\text{exterior}} - \varphi_{\text{interior}} \tag{14}$$

We then graphed porosity contrast against basin diameter to observe the trends in porosity with basin size. We also calculated and graphed the average porosity contrast for all basins formed within a specific epoch of lunar history. All 50 basins formed during the Pre-Nectarian, Nectarian, or Imbrian epochs, so these were the three eras depicted in the porosity-age graph. Porosity values for basin interiors, rims, and exteriors are plotted in Fig. 4. The porosity contrasts (Eq. 14) as a function of basin diameter are plotted in Fig. 5. Finally, porosity contrasts as a function of basin age are plotted in Fig. 6.

2.6. Limitations of methodology and rationale for excluding basins

The analysis that we perform here is most applicable to the geologically simple, FHT basins. For basins that are filled with mare deposits or highly degraded by overlying craters, our analysis did not yield reliable results. The grain density analysis that we use (Wieczorek et al., 2013) relied on extrapolations in the vicinity of mare deposits, and density analyses in these areas may therefore yield unexpected results. Basins that were old and degraded by later-formed craters tended to have scattered porosity signatures that showed a mix of the original basin's porosity and the porosity of the overlying craters, which masked any significant porosity contrasts that might have previously existed. We therefore excluded basins with mare fill or large numbers of overlying craters from the limited-basin analysis (Table 1).

In addition, the geochemical terrane (Jolliff et al., 2000) of a basin could change the way our methods interpreted the porosity. The grain density data set was most accurate for FHT basins. Since the South Pole-Aitken Terrane and the Procellarum KREEP Terrane have different rock compositions from the FHT, we excluded them from the limited-basin

Table 1
Properties of the 50 basins studied.

Basin name	Diameter (km)	Median latitude (° N)	Median longitude (° E)	Epoch of formation	Geochemical terrane (Jolliff et al., 2000)	Interior porosity (%)	95% confidence interval for interior porosity (%)	Rim porosity (%)	95% confidence interval for rim porosity (%)	Exterior porosity (%)	95% confidence interval for exterior porosity (%)	**Porosity contrast (%)**
Birkhoff	345	58.70	−146.1	Pre-Nectarian	FHT,A	16.37	0.028	16.21	0.02	13.49	0.014	**−2.88**
Amundsen-Ganswindt	335	−81	120	Pre-Nectarian	SPA	11.89	0.082	13.53	0.048	15.55	0.028	**3.66**
Schiller-Zucchius	335	−56	−45	Pre-Nectarian	FHT,O	11.70	0.082	16.15	0.048	15.79	0.028	**4.09**
Poincaré	319	−56.70	163.6	Pre-Nectarian	SPA	10.54	0.054	12.34	0.034	12.21	0.014	**1.66**
Planck	314	−57.90	136.8	Pre-Nectarian	SPA	13.48	0.034	13.04	0.028	10.9	0.014	**−2.58**
Mendeleev*	313	5.70	140.9	Nectarian	FHT,A	12.93	0.082	16.26	0.042	17.49	0.02	**4.56**
Schrödinger	312	−75.00	132.4	Imbrian	SPA	16.35	0.042	15.14	0.028	13.15	0.014	**−3.20**
Lorentz*	312	32.60	−95.3	Pre-Nectarian	FHT,A	12.05	0.062	14.51	0.062	18.98	0.028	**6.93**
Sikorsky-Rittenhouse	310	−68	111	Nectarian	SPA	12.73	0.096	16.28	0.082	15.52	0.028	**2.78**
Pingre-Hausen*	300	−56	−82	Pre-Nectarian	FHT,O	14.74	0.096	16.10	0.062	17.24	0.028	**2.50**
Bailly	287	−66.50	−69.1	Nectarian	FHT,O	16.45	0.02	14.77	0.02	13.12	0.006	**−3.33**
Milne*	272	−31.40	112.2	Pre-Nectarian	FHT,O	16.67	0.108	17.06	0.068	15.62	0.068	**−1.05**
Gagarin*	265	−20.20	149.2	Pre-Nectarian	FHT,A	9.95	0.09	13.65	0.054	13.99	0.042	**4.05**
Deslandres	256	−33.10	−4.8	Pre-Nectarian	PKT	16.31	0.19	12.78	0.082	13.21	0.054	**−3.10**
d'Alembert*	248	50.80	163.9	Nectarian	FHT,A	14.21	0.096	16.82	0.062	14.22	0.028	**0.01**
Leibnitz	245	−38.30	179.2	Pre-Nectarian	SPA	8.61	0.3	12.95	0.094	16.36	0.066	**7.75**
Clavius*	245	−58.80	−14.1	Nectarian	FHT,O	12.64	0.062	14.12	0.048	11.23	0.014	**−1.40**
Harkhebi*	237	39.60	98.3	Pre-Nectarian	FHT,A	14.46	0.054	17.17	0.034	15.52	0.02	**1.06**
Van de Graaff	233	−27.40	172.2	Nectarian	SPA	11.23	0.242	10.99	0.128	13.21	0.074	**1.99**
Von Karman M	225	−47.20	176.2	Pre-Nectarian	SPA	7.60	0.268	10.17	0.168	13.11	0.066	**5.51**
Lagrange*	225	−32.30	−72.8	Pre-Nectarian	FHT,O	17.38	0.192	16.43	0.164	18.05	0.062	**0.67**
Pasteur*	224	−11.90	104.6	Pre-Nectarian	FHT,O	13.18	0.144	17.07	0.082	17.73	0.04	**4.55**
Galois*	222	−14.20	−151.9	Pre-Nectarian	FHT,A	15.29	0.116	16.60	0.082	16.14	0.034	**0.85**
Campbell*	219	45.30	151.4	Pre-Nectarian	FHT,A	15.83	0.096	16.48	0.068	18.07	0.034	**2.23**
Landau*	214	41.60	−118.1	Pre-Nectarian	FHT,A	12.88	0.09	14.16	0.056	16.61	0.034	**3.72**
Belkovich	214	61.10	90.2	Nectarian	FHT,A	15.48	0.056	17.15	0.056	16.74	0.028	**1.26**
Schwarzschild	212	70.10	121.2	Nectarian	FHT,A	14.84	0.042	15.44	0.028	11.61	0.014	**−3.23**
Oppenheimer	208	−35.20	−166.3	Nectarian	SPA	12.50	0.34	13.92	0.126	15.73	0.094	**3.24**
Schickard	206	−44.30	−55.3	Pre-Nectarian	FHT,O	8.72	0.204	18.68	0.142	19.51	0.074	**10.79**
Janssen*	199	−45.40	40.3	Pre-Nectarian	FHT,O	12.80	0.11	14.66	0.062	14.03	0.034	**1.24**
Einstein*	198	16.30	−88.7		FHT,A	14.58	0.184	16.07	0.102	17.00	0.062	**2.41**

(*continued on next page*)

Table 1 (*continued*)

Basin name	Diameter (km)	Median latitude (° N)	Median longitude (° E)	Epoch of formation	Geochemical terrane (Jolliff et al., 2000)	Interior porosity (%)	95% confidence interval for interior porosity (%)	Rim porosity (%)	95% confidence interval for rim porosity (%)	Exterior porosity (%)	95% confidence interval for exterior porosity (%)	**Porosity contrast (%)**
Mandel'shtam*	197	5.40	162.4	Pre-Nectarian	FHT,A	13.58	0.186	15.86	0.118	16.45	0.062	**2.87**
Poczobutt*	195	57.10	−98.8	Pre-Nectarian	FHT,A	15.77	0.076	19.39	0.048	18.67	0.028	**2.90**
Maginus*	194	−50.50	−6.3	Pre-Nectarian	FHT,O	11.61	0.172	11.05	0.152	12.23	0.062	**0.62**
Zeeman	190	−75.20	−133.6	Nectarian	SPA	4.02	0.474	11.47	0.128	10.12	0.094	**6.10**
Humboldt*	189	−27.00	80.9	Imbrian	FHT,O	15.72	0.28	15.62	0.11	16.09	0.062	**0.37**
Petavius*	188	−25.10	60.4	Imbrian	FHT,O	14.49	0.312	18.40	0.162	18.05	0.094	**3.56**
Vertregt	187	−19.80	171.10	Pre-Nectarian	SPA	14.58	0.326	11.62	0.198	12.44	0.074	**−2.1**
Tsiolkovskiy	185	−21.20	128.90	Imbrian	FHT,O	12.22	0.186	15.52	0.138	16.07	0.062	**3.84**
Fabry*	184	42.90	100.70	Pre-Nectarian	FHT,A	12.35	0.192	16.83	0.13	17.29	0.068	**4.94**
Fermi	183	−19.30	122.6	Pre-Nectarian	FHT,O	15.73	0.124	17.89	0.068	15.54	0.042	**−0.18**
Tsander*	181	6.20	−149.30	Pre-Nectarian	FHT,A	12.70	0.29	15.84	0.132	15.51	0.062	**2.81**
Von Karman	180	−44.80	175.90	Pre-Nectarian	SPA	4.59	1.01	10.87	0.234	12.44	0.108	**7.86**
Mach*	180	18.50	−149.30	Pre-Nectarian	FHT,A	11.79	0.282	13.75	0.118	14.41	0.062	**2.62**
Schiller	180	−51.90	−39.00	Nectarian	FHT,O	12.21	0.204	16.44	0.136	17.35	0.108	**5.15**
Chebyshev	178	−30.30	−127.20	Nectarian	SPA	13.72	0.152	13.27	0.118	13.74	0.07	**0.02**
Rozhdestvenskiy	177	85.20	−155.40	Pre-Nectarian	FHT,A	8.69	0.344	14.45	0.144	15.93	0.076	**7.24**
Gauss*	177	35.70	79.00	Nectarian	FHT,O	10.72	0.402	17.75	0.164	18.65	0.116	**7.93**
Grimaldi	172	−5.50	−68.30	Pre-Nectarian	PKT	3.45	1.134	12.85	0.24	15.04	0.082	**11.59**
Rowland*	171	57.40	−162.50	Nectarian	FHT,A	9.99	0.248	16.01	0.152	16.44	0.104	**6.45**

Note: Porosity contrast was calculated by subtracting the interior porosity from the exterior porosity, and other values were used to calculate the confidence intervals for the porosity measurements. If the basin was included in the limited-basin analysis, it has an asterisk placed next to its name. Terranes are denoted as PKT (Procellarum KREEP Terrane), FHT (Feldspathic Highlands Terrane), or SPA (South Pole-Aitken Terrane). The Feldspathic Highlands Terrane is split into the outer FHT (FHT,O) and the anorthositic FHT (FHT,A) (Jolliff et al., 2000).

analysis because the grain density might not have been accurate (Table 1).

Lastly, a basin's latitude affected the way we rendered gridded values of gravity and gravity-from-topography. The bulk density calculations were performed using an equirectangular projection of gravity and gravity-from-topography, with values sampled on a grid every 0.1° of latitude and longitude. For most of the Moon, there is limited areal distortion of the pixels described in Section 2; however, since longitude lines become closer together at high latitudes and datapoints tend to overlap, large basins near the poles experienced significant distortion, potentially overrepresenting certain regions and making the results unreliable. This is our rationale for excluding the Bailly, Schwarzschild, and Rozhdestvenskiy basins in the limited-basin analysis (Table 1).

3. Results

3.1. Porosity maps and overall porosity trends

The porosity map of the Lorentz basin in Fig. 3 is representative of our overall results. Lorentz is a geologically simple basin (no mare fill, not obscured by overlying craters) located near the equator. In addition, it is located in the FHT. Given that our method assumed uniform rock composition when estimating grain density and that the composition we used closely resembled that of the FHT, our method was most robust in the simple FHT basins. The Lorentz basin shows a positive porosity contrast of 6.93% (Table 1), with the interior porosity considerably lower than the exterior. This is typical across many basins in the size range we analyzed, with 80% of the basins we studied exhibiting a lower porosity in the interior compared to the exterior (and 76% of the basins showing a statistically significant drop in porosity between the exterior and interior). Porosity maps of all the basins we analyzed are located in Appendix A.

In order to more-effectively synthesize the porosity trends across all basins, we determined the average porosity in the basin interior, rim, and exterior across the 50 basins we studied (Table 2, Fig. 4). The interior porosities are relatively low, around 12%, and the exterior porosities are somewhat higher, around 15%. The porosity values in the interior and exterior are significantly different, as evidenced by the non-overlapping standard errors between the interior and exterior porosity values. However, the rim and exterior porosity values are very similar on average, though the rim porosities are slightly lower than the exterior. This lends credence to our theory that the rim is a transitional region between the interior and exterior that would be affected by geological processes taking place in both the interior and exterior.

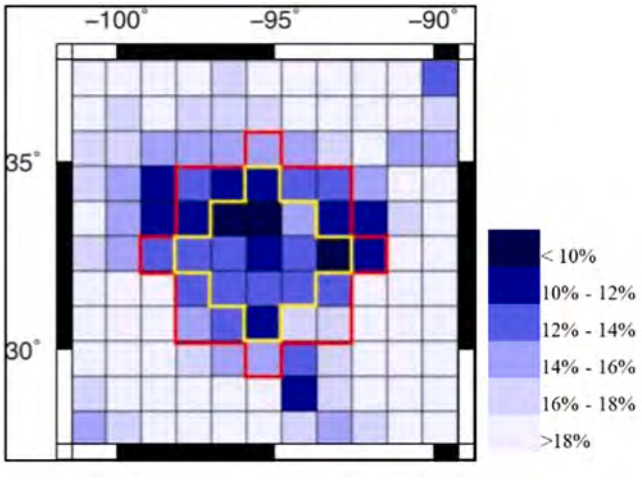

Fig. 3. Porosity map of the Lorentz basin (diameter = 312 km). The Lorentz basin is a Pre-Nectarian basin in the FHT relatively close to the equator. It has a porosity contrast of 6.93%, indicating that the exterior porosity is considerably higher than the interior. This reflects the trend observed among the majority of the basins studied here.

Table 2
Average porosity values across all basins.

Interior average porosity	12.65%
Interior standard deviation	3.20%
Interior standard error	0.46%
Rim average porosity	15.03%
Rim standard deviation	2.20%
Rim standard error	0.31%
Exterior average porosity	15.27%
Exterior standard deviation	2.30%
Exterior standard error	0.33%

Note: Porosity values and corresponding standard deviations and standard errors are given for each annular region over all 50 basins.

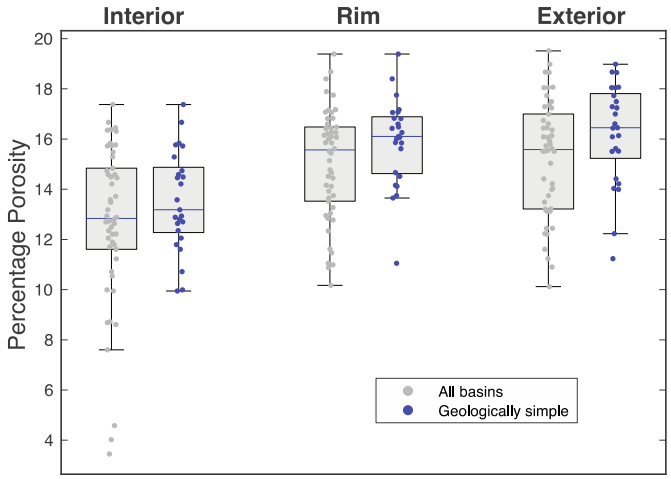

Fig. 4. Box and whisker plot of average porosity in three different regions of the basins: the interior, rim, and exterior. Grey boxes demarcate the 25th, 50th, and 75th percentiles for each category, and outliers are displayed separately. Results are shown for all basins (grey points, the left-hand plot in each pairing) as well as for geologically simple FHT basins (blue points, the right-hand plot in each pairing). (For interpretation of the references to colour in this figure legend, the reader is referred to the web version of this article.)

Our methodology assumes that the crustal grain density is constant in the vicinity of the studied region, so our calculated bulk density values are most reliable in regions with uniform crustal composition, such as the FHT. The interpretation of bulk density and porosity is more complicated within basins that overlap with other basins and large craters, since these basins and craters may impart porosity of their own. Many of the basins that display compositional variations or geologic complexity were observed to have outlier porosity values. For example, the Deslandres basin, a Procellarum KREEP Terrane basin filled with mare deposits, shows a negative porosity contrast, and many basins in the South Pole-Aitken basin (such as Leibnitz and Von Karman M) had unusually low porosity values. These outlier values are likely a result of the assumptions we made in our methodology, and we decided to perform some analyses on the basins that fit our assumptions and exclude the geologically complex basins. The excluded basins are the ones not marked with an asterisk next to the basin name in Table 1.

After excluding the complex basins, we re-analyzed the average porosity in the interior, rim, and exterior of the 25 simple FHT basins (Table 3, Fig. 4). The same overall trends held, with the interior porosity significantly lower than the exterior and the rim with a porosity close to, but lower than, that of the exterior. However, the standard deviation of the results decreased substantially, especially for the interiors, indicating that the simple FHT basins have more-closely clustered porosity

Table 3
Average porosity values for geologically simple FHT basins.

Interior average porosity	13.53%
Interior standard deviation	1.98%
Interior standard error	0.40%
Rim average porosity	15.91%
Rim standard deviation	1.73%
Rim standard error	0.35%
Exterior average porosity	16.23%
Exterior standard deviation	2.00%
Exterior standard error	0.41%

Note: Porosity values and corresponding standard deviations and standard errors are given for each annular region over geologically simple basins in the FHT.

values and that the trend of positive porosity contrasts is more pronounced in these basins. Note that the standard errors did not change substantially when we excluded the complex basins despite the decreasing standard deviations, largely because the number of basins used in the analysis decreased. Overall, the results in the porosity maps and average-porosity graphs indicate that interior porosities tend to be lower than exterior porosities in intermediate-sized basins, and that this trend is more widespread among simple FHT basins.

3.2. Porosity in relation to other geological properties

Similar to the analysis conducted by Soderblom et al. (2015), we have graphed porosity contrast vs. basin diameter in order to see whether porosity changed significantly with diameter (Fig. 5). There was considerable scatter in the data ($r^2 = 0.1012$) when we included all 50 basins (Fig. 5a). In order to see whether the lack of porosity-diameter correlation was due to the geologically complex and non-FHT basins, we excluded all basins not marked with an asterisk in Table 1 and graphed porosity vs. diameter again (Fig. 5b). There was even less correlation in these basins ($r^2 = 0.0049$), indicating that there truly is no correlation between porosity and diameter in this size range. Given that Soderblom et al. (2015) observed more scatter in the porosities of the larger basins in their size range of 27–201 km, it is logical that there continues to be scatter in the data of the even-larger basins we examined here (170–360 km). There are many factors beyond geological terrane that affect porosity, such as age and preimpact porosity, and some of these factors may be contributing to the lack of porosity-diameter correlation in the limited-basin analysis within the diameter range of 170–360 km.

When we analyzed the average porosity contrast for basins formed within each epoch of the lunar geologic timescale, we observed lower porosity within basins relative to the exterior across all time periods (Fig. 6). The Pre-Nectarian (oldest) epoch had the lowest interior porosities (i.e. largest positive porosity contrasts), with the Imbrian (youngest) epoch having higher interior porosities relative to the exterior. This trend was weak, and the high standard deviations in these period-averages indicate that age does not significantly affect porosity. In addition, when we excluded the geologically complex and non-FHT basins, the trend completely disappeared, with the Nectarian basins showing the highest porosity contrasts. This suggests that there is no real correlation between porosity contrast and age in basins 170–360 km in diameter. It appears that the overall trend of lower porosity in interiors compared to exteriors does not significantly vary based on the basin's age or diameter.

4. Discussion

4.1. Physical phenomena affecting porosity

The majority of the basins we studied exhibited a lower porosity in the interior compared to the exterior, a trend that was reflected in our average-porosity calculations for all basins in our size range as well as for just the equatorial, geologically simple highlands basins. This

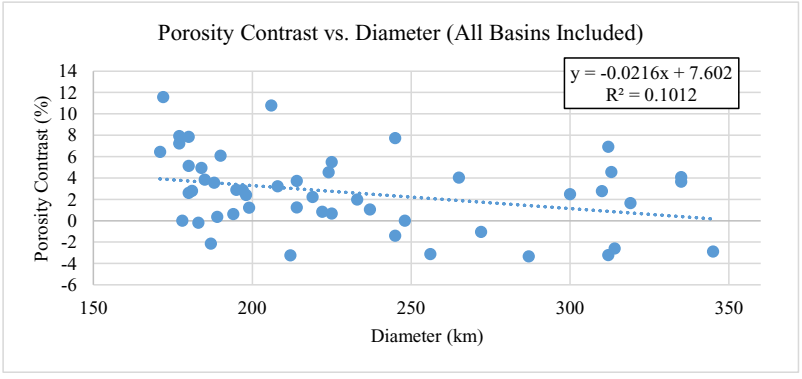

a)

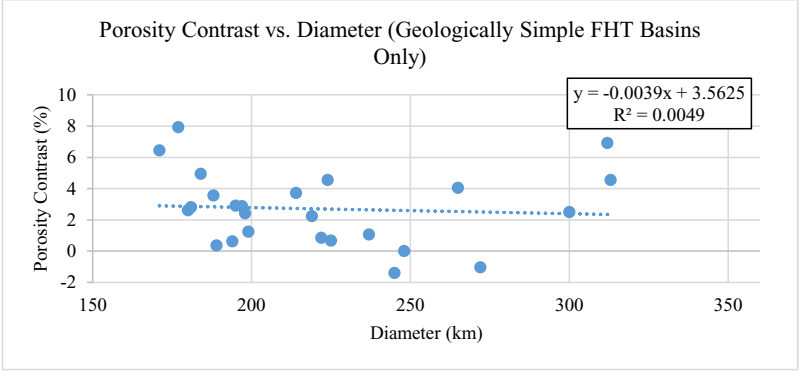

b)

Fig. 5. Porosity contrast vs. diameter, (a) for all basins and (b) for geologically simple FHT basins only.

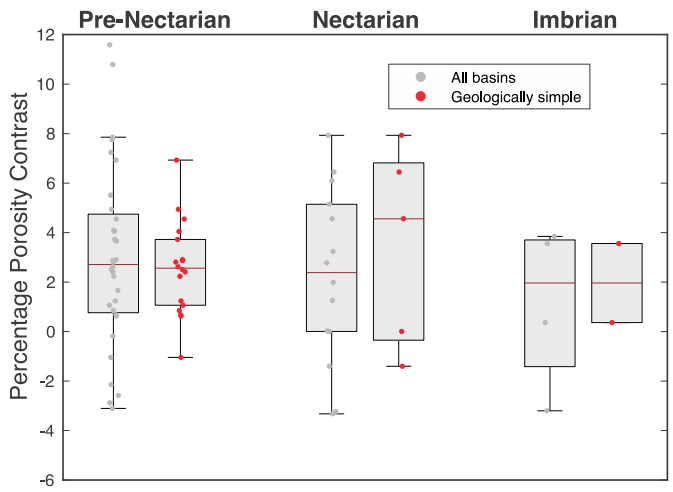

Fig. 6. Box and whisker plot of porosity contrast vs. age. Results are shown for all basins (grey points, the left-hand plot in each pairing) as well as for geologically simple FHT basins (red points, the right-hand plot in each pairing). (For interpretation of the references to colour in this figure legend, the reader is referred to the web version of this article.)

indicates that impact melting, which tends to result in lower porosities, may be the dominant force in the basin interiors. During the impact event, the heat from the impact likely melted a large portion of the Moon's crust within the basin, erasing any preimpact porosity that existed and causing the rock to re-solidify with a much lower porosity. The only porosity in the rock once it re-solidified would be a result of gas bubbles in the molten rock (Milbury et al., 2015), which would yield porosity values similar to those observed in the interior of the basins in this study.

Given the size of the basins we studied, impact scaling laws predict that the rock in the uppermost kilometers of the basin interiors should be composed of low-porosity impact melt. Analysis of the 390-km impact melt sheet (slightly larger than the basins in our size range) within the 930-km Orientale basin indicates that large volumes of impact melt, on the order of 10^5 km^3, may be formed during impact events that create basins roughly 300 km in diameter (Vaughan et al., 2013). The majority of this impact melt remains within the interior of the resulting basin, and in Orientale's case, the impact melt sheet is approximately 15 km thick. The amount of impact melt produced scales with the size of a basin, so it is possible that the impact melt sheets in the smaller basins studied by Soderblom et al. (2015) may have been too thin to considerably affect the interior porosity. However, it is likely that thick impact melt sheets are present in the basins we examined and would have generated low porosities in the basin interiors, at least to depths of a few kilometers.

Based on the results of Wiggins et al. (2019), it appears that the outer bound of the exterior region is likely still within the area affected by fracturing/dilatancy and a continuous ejecta blanket. The exterior porosity is likely a combination of fractured material from the shock wave that passed through the rock and the porous ejecta deposited outside the basin rim. The heat from the impact event decreases with distance from the center of the basin, so there would be no major melting mechanisms that would decrease porosity and counteract the mechanisms of fracturing and ejecta emplacement in the basin exterior. The fact that the rim porosities are close to the exterior on average indicates that impact melting does not extend beyond the center of the basin, and that fracturing occurs throughout the basin and surrounding region and is only observed when the effect of impact melting is minimal.

The low porosities observed across all of these basins are consistent with the observations of larger basins made by Wieczorek et al. (2013). This is to be expected since our methodology is broadly similar to theirs, in the sense that both methodologies rely on an analysis of short-wavelength GRAIL and LOLA data.

Since Soderblom et al. (2015) had found a significant trend between porosity and basin diameter, we had proposed that we might find a similar trend between porosity contrast and basin diameter in the basins we studied. However, we did not find any significant trend, and the correlation decreased when we excluded the geologically complex basins. This could be for a number of reasons. The larger basin sizes correlate with older, more-degraded basins with obscured porosity signatures. Alternatively, the size range we studied might be a transitional range between the high interior porosities observed by Soderblom et al. (2015) and the low interior porosities observed by Wieczorek et al. (2013) that exhibits some of the characteristics of each of the other size ranges.

When we studied the relationship between *interior* porosity and basin diameter (which, if a correlation existed, might indicate that the depth of melting in the interior of a basin depends on the basin's diameter), we found a similarly weak linear correlation, with $r^2 = 0.0628$. The fact that no correlation between interior porosity and diameter exists lends credence to our theory that the upper kilometers of the crust are subject to melting phenomena during the formation of an impact basin in the size range we analyzed.

Similarly, there did not appear to be a correlation between porosity and basin age. Although we believed that changing impact conditions and preimpact porosity (Milbury et al., 2015) might have contributed to the porosity signatures, there did not appear to be such a trend. Perhaps the natural variability in geologic properties across different terrains masked any age trend that might otherwise have existed. Scatter in Bouguer anomalies and porosity values due to impact conditions and local environments has also been observed for smaller craters (especially those outside the highlands), so it may be expected that this type of scatter would exist in the larger basins we examined (Bierson et al., 2016).

4.2. Depth sensitivity

Although our analysis calculates a scalar value for bulk density and porosity for a given geographic region, the reality is that bulk density and porosity are expected to vary strongly with depth in the lunar interior. A spatio-spectral analysis of gravity and topography over the lunar highlands by Besserer et al. (2014) revealed that the porosity of the uppermost kilometer of the Moon's crust is generally in the range of 25–30% but that the porosity shrinks to nearly zero at tens of kilometers' depth. Consequently, our scalar values of bulk density and porosity represent a convolution of the true values across a range of depths.

A mass sheet σ at a depth d produces a free-air gravity anomaly δg at the surface ($r = R_0$), and the spherical harmonic coefficients of these quantities are related as follows:

$$\delta g_{lm} = 4\pi G\rho\left(\frac{l-1}{2l+1}\right)\left(\frac{R_0-d}{R_0}\right)^{l+2}\sigma_{lm} \tag{15}$$

Meanwhile, the gravity produced by an identical mass sheet at the surface would have the following amplitude:

$$\delta g_{lm} = 4\pi G\rho\left(\frac{l-1}{2l+1}\right)\sigma_{lm} \tag{16}$$

The gravity coming from the deeper mass sheet is always weaker due to the phenomenon of upward continuation. For a given spherical harmonic degree, we can define the mass sheet depth d_{half} at which gravity is attenuated by a factor of ½ as:

$$d_{half} = R_0\left[1-\left(\frac{1}{2}\right)^{\frac{1}{l+2}}\right] \tag{17}$$

For the lowest spherical harmonic degree fully included in our band-pass ($l = 250$), this depth is 4.8 km. Therefore, the band-pass described in Section 2.1 is primarily sensitive to the uppermost 5 km of the lunar crust, with a lesser contribution from the middle crust. Crucially, all bulk

density values presented in this paper have comparable depth sensitivity, which allows for comparisons between regions.

The total depth sensitivity S of our bulk density method may be quantified more thoroughly by calculating a weighted mean of gravity from a mass sheet across all spherical harmonic degrees in our band pass, following the methodology of Wieczorek and Phillips (1997):

$$S(d) = \sum_l \omega(l) l^{-2} \left(\frac{R_0 - d}{R_0}\right)^{l+2} \Big/ \sum_l \omega(l) l^{-2} \quad (18)$$

where $\omega(l)$ is the windowing function given in Eq. 1. This depth sensitivity (plotted in Fig. 7) gives the expected contribution of subsurface mass anomalies to the external gravity field, normalized by the contribution of a similar mass sheet at zero depth. This depth sensitivity can be compared to that of Soderblom et al. (2015). Since the half-wavelength of a basin's Bouguer anomaly approximately corresponds to its diameter, we can associate basins of various sizes with a representative spherical harmonic degree ($l = 55$ for diameters of D = 100 km and $l = 27$ for diameters of D = 200 km). This yields depth sensitivities that are much higher in the lower crust (see Fig. 7), indicating that the analysis of Soderblom et al. was more sensitive to deep porosity variations than our methodology.

4.3. Reconciliation with previous studies

This work bridges the gap between previous studies that analyzed porosity trends in small basins (Soderblom et al., 2015) and in large basins (Wieczorek et al., 2013). While Soderblom et al. reported the presence of a negative porosity contrast (i.e., higher porosity in the interior than the exterior) for 200-km-diameter basins, Wieczorek et al. reported that basins larger than approximately 360 km had a positive porosity contrast. Taken at face value, these two studies would suggest that a transition in the distribution of porosity occurs for intermediate-sized basins. However, we find no such transition in the basins studied here; rather, we find that basins of all diameters within our size range tend toward a positive porosity contrast. This is consistent with the results of Wieczorek et al., but it is in conflict with the results of Soderblom et al.

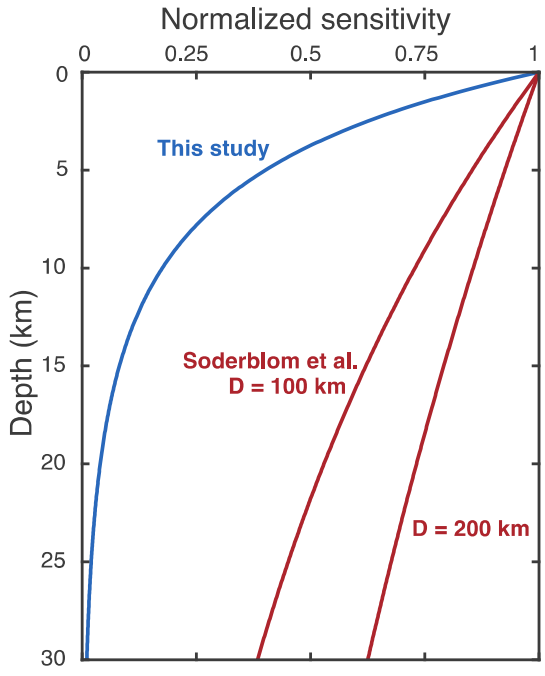

Fig. 7. Normalized depth sensitivity for this study (black), and for Soderblom et al. (grey) for crater diameters of D = 100 km and D = 200 km.

Why does this discrepancy exist? We propose three possible explanations: first, there may be too few basins in the size range we studied to provide a significant correlation (we studied 50 basins compared to Soderblom et al.'s 1185 basins, and we were only left with 25 basins once we excluded the geologically complex basins). Second, it should be noted that these studies invoke differing assumptions about the Moon's interior, some of which may be overly simplistic. For example, our work and that of Wieczorek et al. require gravity and topography to be locally "stationary" processes (Wieczorek and Simons, 2007). Therefore, any geologic variability within a given pixel or window may yield unexpected results; it should be noted that the relatively small pixel size of this work makes our analysis less susceptible to geologic complexity than the broad Slepian window of Wieczorek et al. In contrast, the analysis of Soderblom et al. incorporated a priori assumptions about the mean bulk density of the crust and about the onset of mantle uplift.

Third, it is possible to reconcile these studies by considering the differing depth sensitivities of these analyses. As demonstrated in Fig. 7, our bulk density analysis is primarily sensitive to the uppermost several kilometers of the lunar crust. Meanwhile, the Residual Bouguer Anomalies (RBAs) analyzed by Soderblom et al. are influenced by the presence of porosity throughout the entire crust, as demonstrated by the red curves in Fig. 7. Therefore, our analysis may be reconciled with that of Soderblom et al. if the shallow subsurface in a basin interior has low porosity, whereas the deeper subsurface in the same region has relatively high porosity. Such a scenario might be actualized by the presence of deep fracture-induced porosity that is overlain by relatively shallow impact melting. The RBAs reported by Soderblom et al. may also imply that the high "exterior" porosities observed in our paper are confined to relatively shallow depths.

4.4. Future research

Since our methodology of using a least-squares fit between gravity and gravity-from-topography to calculate density is applicable to basins of all sizes, we might consider applying this methodology to basins of all sizes in order to see trends across a wider diameter range without contending with the different assumptions made by different methodologies. Additional basins with a diameter over 360 km should be tested with the current methodology to test whether they are consistent with the results of Wieczorek et al. (2013), and similarly with smaller basins studied by Soderblom et al. (2015) to understand the inconsistency better, before we make broader conclusions about porosity in different diameter ranges.

In any case, this work serves as a proof of concept for a methodology that can be applied to a variety of lunar geology studies. While we chose square "pixels" here for the sake of broadly characterizing basin-related porosity, the Nettleton method may be applied for an arbitrarily shaped study region. Therefore, the "recipe" provided in Section 2.4 may be customized in the future for more focused studies of lunar landforms.

5. Conclusion

The methods used in this study were a new approach to calculating porosity that may be applied to terrains of all sizes. In this paper, we specifically assessed geographic trends in porosity near intermediate-sized basins. We found low porosities in the interiors of a majority of these basins, most likely due to impact melting, and comparably higher porosities in the ejecta-influenced, fractured exteriors. This confirms our primary hypothesis that porosity would change significantly between the interiors and exteriors of the basins. We did not observe any significant trends between porosity and basin diameter or age among intermediate-sized craters.

In the context of previous studies, this work reveals a portrait of the crust underneath lunar impact basins: impacted-induced fracturing and dilatancy underneath a basin produces high values of porosity down to depths of several to tens of kilometers. The uppermost kilometers of the

crust under the interior of a basin have relatively low porosity, likely due to pore-space closure associated with impact heating and/or melting. Given that we observe no apparent diameter-dependence of porosity in basin interiors, we conclude that these mechanisms for porosity reduction extend to depths of at least a few kilometers for all basin diameters in this study (170–360 km). The shallow crust of a basin exterior has high porosity, resulting from some undetermined combination of impact fracturing and unconsolidated impact ejecta. The shallow crust of a basin rim typically has porosity values similar to those of the exteriors, indicating that fracturing and ejecta deposition were the dominant phenomena in the uppermost kilometers of the basin rim. This portrait affirms recent numerical impact simulations (Wiggins et al., 2019) and illuminates mechanisms by which the lunar crust acquired porosity throughout its history of bombardment.

In coordination with numerical modeling of impact events, these results may help determine the different properties and conditions of ancient impact events, such as the physical phenomena acting in different areas of basins during formation. Future impact models will need to confirm the empirical observations recorded in this study and understand the causes of the porosity trends observed here. This study contributes to the growing research on lunar impact basins that aims to define the bombardment conditions in the early Solar System, which shaped the evolution of the Moon as well as Earth.

Declaration of Competing Interest

The authors do not have any competing interests to declare.

Acknowledgements

T. K. V. acknowledges the support of the Ardsley High School Science Research program, in which she participated while conducting this research, and its founder, Mrs. Diana Evangelista. P. B. J. was supported by NASA's GRAIL science team and the Urey Fellows program at the Lunar and Planetary Institute.

Appendix A. Supplementary data

Datasets related to this article can be found at https://dataverse.harvard.edu/dataset.xhtml?persistentId=doi:10.7910/DVN/R2DQBC, hosted at Harvard Dataverse (Venkatadri and James, 2020). Supplementary data to this article can be found online at https://doi.org/10.1016/j.icarus.2020.113953.

References

Andrews-Hanna, J.C., Asmar, S.W., Head, J.W., Kiefer, W.S., Konopliv, A.S., Lemoine, F. G., Matsuyama, I., Mazarico, E., McGovern, P.J., Melosh, H.J., Neumann, G.A., 2013. Ancient igneous intrusions and early expansion of the moon revealed by GRAIL gravity gradiometry. Science 339 (6120), 675–678.

Audet, P., 2014. Toward mapping the effective elastic thickness of planetary lithospheres from a spherical wavelet analysis of gravity and topography. Phys. Earth Planet. Inter. 226, 48–82.

Besserer, J., Nimmo, F., Wieczorek, M.A., Weber, R.C., Kiefer, W.S., McGovern, P.J., Andrews-Hanna, J.C., Smith, D.E., Zuber, M.T., 2014. GRAIL gravity constraints on the vertical and lateral density structure of the lunar crust. Geophys. Res. Lett. 41 (16), 5771–5777.

Bierson, C.J., Phillips, R.J., Nimmo, F., Besserer, J., Milbury, C., Keane, J.T., Soderblom, J.M., Zuber, M.T., 2016. Interactions between complex craters and the lunar crust: analysis using GRAIL data. Journal of Geophysical Research: Planets 121 (8), 1488–1497.

Blewett, D.T., Hawke, B.R., Lucey, P.G., 2002. Lunar pure anorthosite as a spectral analog for mercury. Meteorit. Planet. Sci. 37 (9), 1245–1254.

Collins, G.S., 2014. Numerical simulations of impact crater formation with dilatancy. Journal of Geophysical Research: Planets 119 (12), 2600–2619.

Dahlen, F.A., Simons, F.J., 2008. Spectral estimation on a sphere in geophysics and cosmology. Geophys. J. Int. 174 (3), 774–807.

Gillis, J.J., Jolliff, B.L., Korotev, R.L., 2004. Lunar surface geochemistry: global concentrations of Th, K, and FeO as derived from lunar prospector and Clementine data. Geochim. Cosmochim. Acta 68 (18), 3791–3805.

Harig, C., Lewis, K.W., Plattner, A., Simons, F.J., 2015. A suite of soft analyzes data on the sphere. Eos. 96 (6), 18–22.

Huang, Q., Wieczorek, M.A., 2012. Density and porosity of the lunar crust from gravity and topography. Journal of Geophysical Research: Planets 117 (E5).

Johnson, B.C., Bowling, T.J., 2014. Where have all the craters gone? Earth's bombardment history and the expected terrestrial cratering record. Geology 42 (7), 587–590.

Jolliff, B.L., Gillis, J.J., Haskin, L.A., Korotev, R.L., Wieczorek, M.A., 2000. Major lunar crustal terranes: surface expressions and crust-mantle origins. Journal of Geophysical Research: Planets 105 (E2), 4197–4216.

Losiak, A., Wilhelms, D.E., Byrne, C.J., Thaisen, K.G., Weider, S.Z., Kohout, T., O'Sullivan, K., Kring, D.A., 2009, March. A new lunar impact crater database. In: Lunar and Planetary Science Conference, 40.

Milbury, C., Johnson, B.C., Melosh, H.J., Collins, G.S., Blair, D.M., Soderblom, J.M., Nimmo, F., Bierson, C.J., Phillips, R.J., Zuber, M.T., 2015. Preimpact porosity controls the gravity signature of lunar craters. Geophys. Res. Lett. 42 (22), 9711–9716.

Miljković, K., Wieczorek, M.A., Collins, G.S., Laneuville, M., Neumann, G.A., Melosh, H. J., Solomon, S.C., Phillips, R.J., Smith, D.E., Zuber, M.T., 2013. Asymmetric distribution of lunar impact basins caused by variations in target properties. Science 342 (6159), 724–726.

Nettleton, L.L., 1939. Determination of density for reduction of gravimeter observations. Geophysics 4 (3), 176–183.

Neumann, G.A., Zuber, M.T., Wieczorek, M.A., Head, J.W., Baker, D.M., Solomon, S.C., Smith, D.E., Lemoine, F.G., Mazarico, E., Sabaka, T.J., Goossens, S.J., 2015. Lunar impact basins revealed by gravity recovery and interior laboratory measurements. Sci. Adv. 1 (9), e1500852.

Parasnis, D.S., 1952. A study of rock densities in the English midlands. Geophysical Supplements to the Monthly Notices of the Royal Astronomical Society 6 (5), 252–271.

Smith, D.E., Zuber, M.T., Neumann, G.A., Lemoine, F.G., Mazarico, E., Torrence, M.H., McGarry, J.F., Rowlands, D.D., Head, J.W., Duxbury, T.H., Aharonson, O., 2010. Initial observations from the lunar orbiter laser altimeter (LOLA). Geophys. Res. Lett. 37 (18).

Soderblom, J.M., Evans, A.J., Johnson, B.C., Melosh, H.J., Miljković, K., Phillips, R.J., Andrews-Hanna, J.C., Bierson, C.J., Head, J.W., Milbury, C., Neumann, G.A., 2015. The fractured moon: production and saturation of porosity in the lunar highlands from impact cratering. Geophys. Res. Lett. 42 (17), 6939–6944.

Sori, M.M., 2018. A thin, dense crust for mercury. Earth Planet. Sci. Lett. 489, 92–99.

Talwani, M., Thompson, G., Dent, B., Kahle, H.G., Buckc, S., 1973. 13. Traverse Gravimeter Experiment. Apollo 17: Preliminary Science Report, p. 330.

Thompson, J.K., Tree, D.R., 1980. Leakage error in fast Fourier analysis. J. Sound Vib. 71 (4), 531–544.

Vaughan, W.M., Head, J.W., Wilson, L., Hess, P.C., 2013. Geology and petrology of enormous volumes of impact melt on the moon: a case study of the Orientale basin impact melt sea. Icarus 223 (2), 749–765.

Venkatadri, T.K., James, P.B., 2017. Relatively low porosities detected within lunar Farside basins. In: Lunar and Planetary Science Conference, 48.

Venkatadri, T.K., James, P.B., 2020. Variations of Porosity in Intermediate-Sized Lunar Impact Basins: Datasets and Supplementary Materials. Harvard Dataverse, p. v1. https://doi.org/10.7910/DVN/R2DQBC.

Wieczorek, M.A., 2007. Gravity and topography of the terrestrial planets. Treatise on Geophysics 10, 165–206.

Wieczorek, M.A., Meschede, M., 2018. Shtools: tools for working with spherical harmonics. Geochem. Geophys. Geosyst. 19 (8), 2574–2592.

Wieczorek, M.A., Phillips, R.J., 1997. The structure and compensation of the lunar highland crust. Journal of Geophysical Research: Planets 102 (E5), 10933–10943.

Wieczorek, M.A., Phillips, R.J., 1998. Potential anomalies on a sphere: applications to the thickness of the lunar crust. Journal of Geophysical Research: Planets 103 (E1), 1715–1724.

Wieczorek, M.A., Simons, F.J., 2007. Minimum-variance multitaper spectral estimation on the sphere. J. Fourier Anal. Appl. 13 (6), 665–692.

Wieczorek, M.A., Neumann, G.A., Nimmo, F., Kiefer, W.S., Taylor, G.J., Melosh, H.J., Phillips, R.J., Solomon, S.C., Andrews-Hanna, J.C., Asmar, S.W., Konopliv, A.S., 2013. The crust of the moon as seen by GRAIL. Science 339 (6120), 671–675.

Wiggins, S.E., Johnson, B.C., Bowling, T.J., Melosh, H.J., Silber, E.A., 2019. Impact fragmentation and the development of the deep Lunar Megaregolith. Journal of Geophysical Research: Planets 124, 941–957.

Yamamoto, A., 1999. Estimating the optimum reduction density for gravity anomaly: a theoretical overview. Journal of the Faculty of Science, Hokkaido University 11 (3), 577–599. Series 7, Geophysics.

Zuber, M.T., Smith, D.E., Watkins, M.M., Asmar, S.W., Konopliv, A.S., Lemoine, F.G., Melosh, H.J., Neumann, G.A., Phillips, R.J., Solomon, S.C., Wieczorek, M.A., 2013. Gravity field of the moon from the gravity recovery and interior laboratory (GRAIL) mission. Science 339 (6120), 668–671.